LANGMUIR

pubs.acs.org/Langmuir Article

Nanoscale Thin-Film Boiling Processes on Heterogeneous Surfaces

Shan Gao,* Jian Qu, Zhichun Liu,* and Wei Liu

Cite This: *Langmuir* 2022, 38, 6352−6362 Read Online

ACCESS | Metrics & More | Article Recommendations | Supporting Information

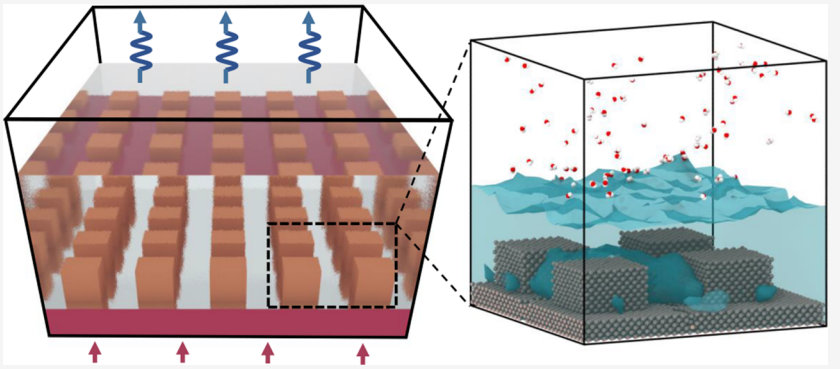

ABSTRACT: Acquiring rapid and efficient boiling processes has been the focus of industry as they have the potential to improve the energy efficiency and reduce the carbon emissions of production processes. Here, we report nanoscale thin-film boiling on different heterogeneous surfaces. Through nonequilibrium molecular dynamics simulation, we captured the triple-phase interface details, visualized the bubble nucleation, and recorded the internal fluid flow and thermal characteristics. It is found that nanoscale thin-film boiling without the occurrence of bubble nucleation shows excellent heat and mass transfer performance, which differs from macroscale boiling. In general, rough structures advance the onset time of stable boiling and improve the efficiency. The heat transfer coefficient and heat flux on a rough hydrophilic surface respectively reach to 7.43×10^4 kW/(m^2·K) and 1.3×10^6 kW/m^2 at a surface temperature of 500 K, which are 100-fold higher than those of micrometer-scale thin-film boiling. However, due to the resultant vapor film trapped between the liquid and the surface, the rough hydrophobic surface leads to heat transfer deterioration instead. It is revealed that the underlying mechanism of regulatory effects resulting from surface physicochemical properties is originated from the variation of interfacial thermal resistance. It is available to reduce the overall interfacial resistance and further improve the heat and mass transfer efficiency through increasing surface roughness, enhancing surface wettability, and increasing the area proportion of the hydrophilic region. This work provides guidelines to achieve rapid and efficient thin-liquid-film boiling and serves as a reference for the optimized design of surfaces utilized for high-heat flux removal through vaporization processes.

1. INTRODUCTION

Boiling is a pervasive phase transition phenomenon and has widespread industrial applications, such as power generation,[1] microelectronic device cooling,[2,3] and chemical processing.[4] Especially in the energy conversion and utilization systems, boiling processes are widely utilized for enhancing heat transfer performance; thus, it is of great significance to acquire more rapid and efficient boiling for the improvement of energy efficiency.

Recently, the development of micro-/nanomanufacturing technology facilitates the production of engineered surfaces with composite micro-/nanostructures. Owing to the distinctive properties for promising applications in various fields, these composite structures have attracted increasing attention of surface engineers in recent years.[5−7] The experimental studies also reveal that these multiscale structures are important to enhance the liquid−vapor phase change,[8−16] where the heat transfer coefficient (HTC) as a ratio of the heat flux q and the wall superheat ΔT is usually adopted to evaluate the thermal performance. Wen *et al.*[17] developed a two-level hierarchical surface with patterned copper nanowire arrays, which demonstrates a 185% higher boiling HTC as compared with a plain copper surface. Dai *et al.*[18] experimentally and theoretically showed the decoupled effects of the surface structure and wettability by conducting pool boiling experiments on TiO_2 film-coated copper meshes. These enhancement methods seem numerous and diverse but are essentially developed by manipulating the bubble dynamics[19,20] during nucleate boiling. In the macroscale pool boiling, bubbles are

Received: February 2, 2022
Revised: March 18, 2022
Published: May 10, 2022

https://doi.org/10.1021/acs.langmuir.2c00276
Langmuir 2022, 38, 6352−6362

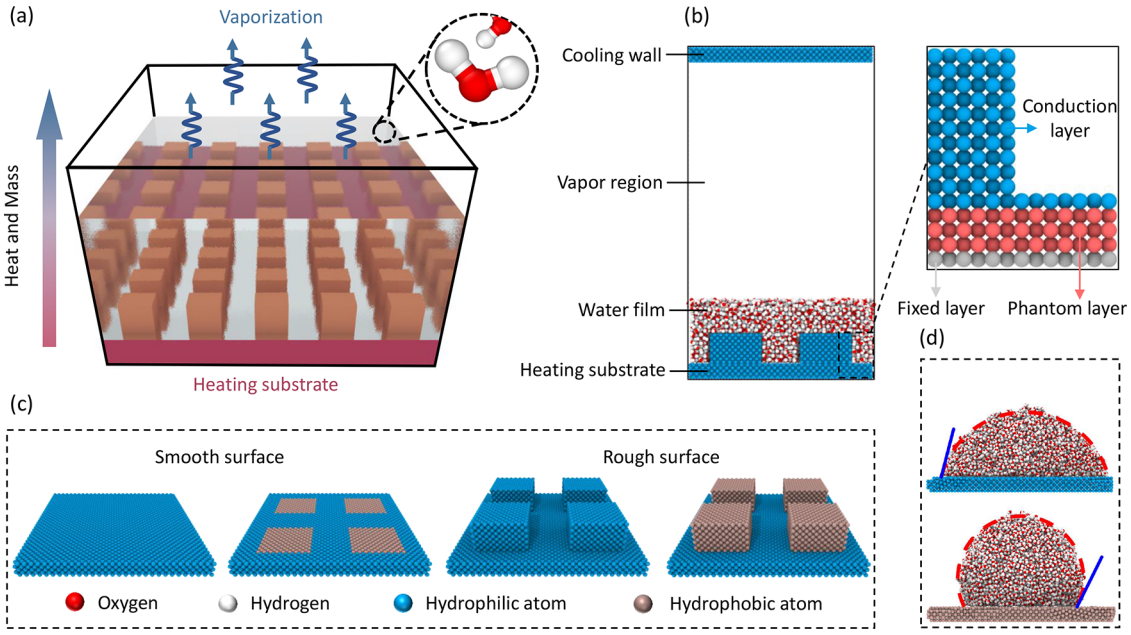

Figure 1. (a) Schematic illustration of the boiling process. The bulk liquid absorbs heat from the substrate to vaporize intensely; this is a representative phenomenon involving heat and mass transfer. (b) Initial configuration of the simulation domain in a vertical section. The working fluid moves from the hot side (bottom substrate) to the cold side (upper wall) by evaporation and condensation. The partially enlarged view shows the arrangement of solid surface atoms. (c) Topography of the four groups of surfaces used in this study: a smooth homogeneous surface with uniform wettability, a smooth heterogeneous surface with hybrid wettability regions, a rough homogeneous surface with uniform wettability, and a rough heterogeneous surface with hybrid wettability pillars. The hybrid wettability region is a 3.07 nm square pattern, and the nanopillar has the same size of width W = 3.07 nm, spacing S = 2.35 nm, and height H = 1.81 nm. (d) Wetting morphology of the droplet and calculation of the contact angle, which characterizes the intrinsic wettability of the hydrophilic surface and the hydrophobic surface used herein.

the gaseous domains on the active nucleation sites of surfaces, they experience nucleation, formation, growth, and departure in their lifetime, and the boiling heat transfer is dominated by these bubble dynamics behaviors. It is found that the HTC can be increased by increasing the nucleation site density, enhancing the bubble growth rate, and accelerating the bubble departure frequency. Therefore, to properly control the bubble behaviors and then guide us to acquire a more efficient boiling, intensive efforts have been devoted to investigating the underlying mechanism of bubble dynamics.[21,22] However, the direct observation and evaluation of the boiling bubble behavior by experiments remain a great challenge due to the nanoscale size of initial bubble nuclei. A molecular-scale understanding of the dynamics, the controlling factors, and the mechanisms of boiling bubbles is crucial to design rapid and efficient boiling processes. Although some numerical studies on boiling have been conducted through molecular dynamics (MD) simulations in the past decade,[23−28] the intuitive visualization and observation of bubble nucleation and growth are lacking, and the mechanism of the initial bubble behaviors merits an in-depth interpretation.

Compared with the boiling of the bulk liquid, thin-film boiling[1,29,30] is quite different, and its faster vaporization and higher heat transfer have attracted increasing attention in the past few years. Wang and Chen[31] utilized nanoporous membranes to realize thin-film boiling and obtained a high heat flux of over 1.2 kW/cm^2, which exceeds the theoretical limit when the liquid layer thickness is estimated to be tens of micrometers. It is revealed that the heat flux increases as the thickness of the liquid film decreases, so it becomes interesting to figure out the following: what is the upper limit of boiling heat flux and how does the heat and mass transfer of nanoscale thin-film boiling perform? Both the surface structure and wettability are critical for boiling processes, and most surfaces in nature are not flat and homogeneous, so it comes to this question: will the heterogeneous nanostructured surfaces with hybrid wettability enhance or reduce nanoscale thin-film boiling? However, we note that few studies have focused on nanoscale thin-film boiling on chemically and physically heterogeneous surfaces, and the bubble dynamics of this boiling process may be distinct and needs to be elucidated clearly.

Unlike traditional computational fluid dynamics simulations, the MD method can directly explore the nanoscopic origins, elucidate phenomena from a molecular perspective, and provide a fundamental understanding that is not accessible by experiments; thus, it has been widely used to investigate various interfacial phenomena, such as droplet wetting,[32,33] impact,[34−37] coalescence,[38,39] and evaporation,[40,41] as well as liquid boiling[42−47] and vapor condensation.[32,48−52] In this paper, nonequilibrium molecular dynamics simulations were performed to investigate the nanoscale thin-film boiling process. Aiming at understanding the initial bubble behaviors and the heat and mass transfer performance, this work was conducted and illustrated around the following objectives: (1) capturing the triple-phase interface to record the lifetime of nanobubbles, (2) visualizing the internal fluid flow and thermal characteristics, (3) studying the effects of surface physico-chemical properties on boiling performance, and (4) revealing the essential regulation mechanism.

2. METHODS

The schematic view of the boiling process is shown in Figure 1a, where a heated substrate is submerged in a stagnant liquid pool. Boiling is an energy transfer process coupled with mass transfer,

https://doi.org/10.1021/acs.langmuir.2c00276
Langmuir 2022, 38, 6352−6362

Table 1. The Physicochemical Properties of Each Simulated Surface

	designation	property
smooth surfaces	S_o	uniformly hydrophobic
	S_i	uniformly hydrophilic
	S_{io}	hydrophilic substrate with hydrophobic patterns
	S_{oi}	hydrophobic substrate with hydrophilic patterns
rough surfaces	R_o	uniformly hydrophobic
	R_i	uniformly hydrophilic
	R_{io}	hydrophilic substrate with hydrophobic structures
	R_{oi}	hydrophobic substrate with hydrophilic structures

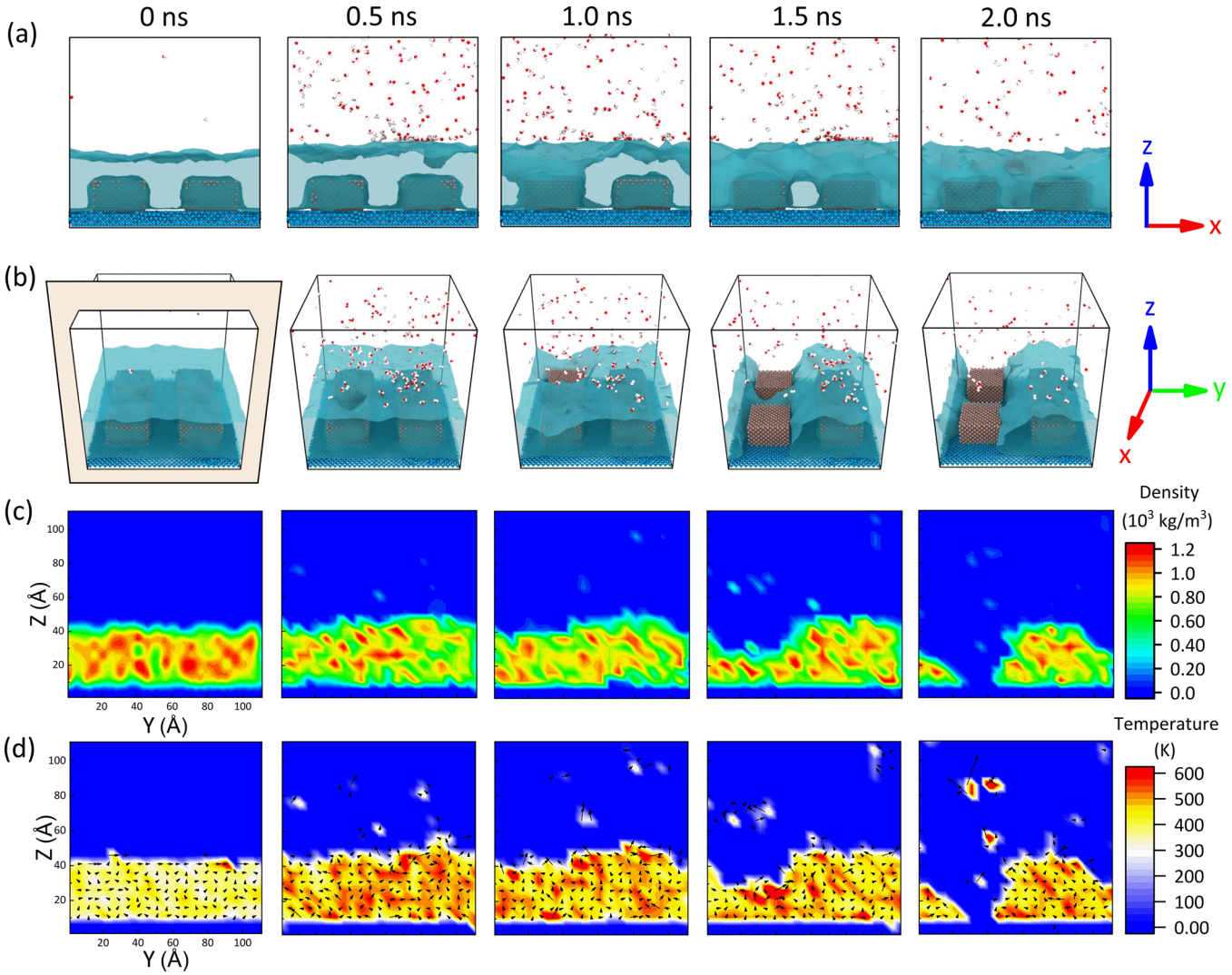

Figure 2. Time-lapse snapshots of the boiling process for the surface R_{io} (rough surface with a hydrophilic substrate and hydrophobic nanopillars). (a) Front view, the top half of the simulation domain is hidden, and the gas−liquid interface is visualized to observe the morphological change of the liquid film more intuitively. (b) Perspective view, the first snapshot schematically shows the cross section used to analyze fluid characteristics. (c) Fluid density contour in the y−z central cross section (x_0 = 56 Å). (d) Fluid temperature contour and velocity field in the y−z central cross section (x_0 = 56 Å).

where the temperature difference drives heat transfer from the underlying surface to the bulk liquid, accompanied by an intense vaporization phenomenon. As shown in Figure 1b, we built and conducted classical MD simulations to study the heat transfer and mass transfer performance of the nanoscale thin-film boiling process and the influence of the surface structure and intrinsic wettability. To prevent the increasing vapor molecules aggregating in the upper region and further restraining the evaporation rate at the gas−liquid interface, we constructed a cooling wall in the upper boundary to condense a part of vaporized molecules, and the distance between the heating substrate and the cooling wall was large enough to eliminate the influences of the generated condensate. The simulation domain had a size of 11.2 nm, 11.2 nm, and 21.2 nm in the x, y, and z directions, respectively. The periodic boundaries were applied in the horizontal directions (the x and y directions), and the z direction of

https://doi.org/10.1021/acs.langmuir.2c00276
Langmuir 2022, 38, 6352−6362

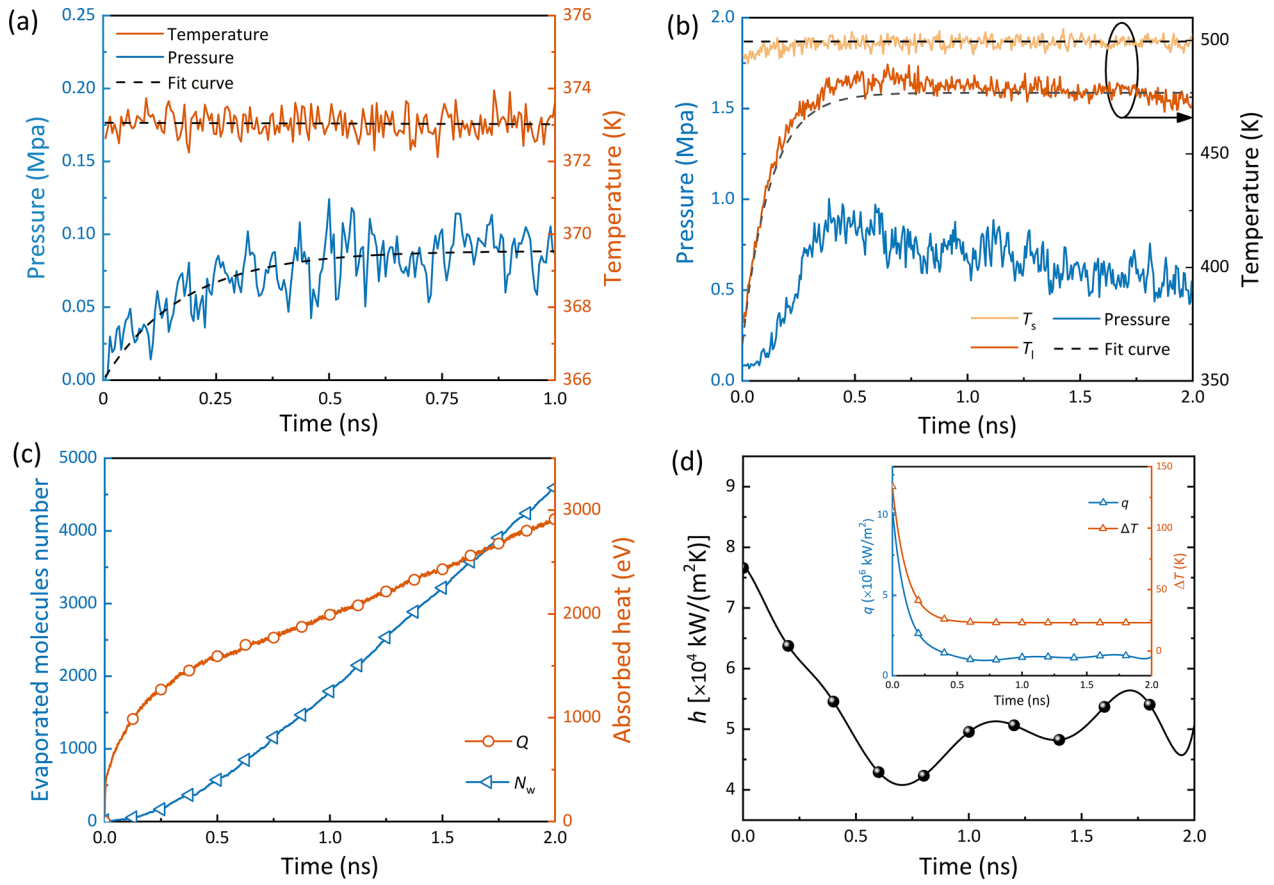

Figure 3. Thermophysical properties of the boiling process for the surface R_{io}. (a) Temporal evolution of liquid film temperature and vapor pressure in the pre-equilibration stage. (b) Temporal evolution of liquid film temperature T_l, heating substrate temperature T_s, and vapor pressure in the main simulation stage (boiling stage). (c) Variation of the number of evaporated molecules N_w and absorbed heat Q of the liquid film. (d) Variation of the surface heat transfer coefficient h, the inset shows the corresponding variations of heat flux q and the temperature difference ΔT between the heating substrate and the liquid film.

the system was set to be a fixed boundary condition with reflecting walls.

Water was used as a working fluid to construct the liquid film with a thickness of about 4 nm, and to ensure comparability among all cases, the total number of water molecules was fixed at 10,170. We chose the TIP4P model to acquire the liquid and vapor properties exactly, where its potential function includes an intermolecular interaction term and a Coulombic force term, as shown in the following expression:

$$U = 4\varepsilon_{OO}\left[\left(\frac{\sigma_{OO}}{r_{ia}r_{jb}}\right)^{12} - \left(\frac{\sigma_{OO}}{r_{ia}r_{jb}}\right)^{6}\right]_{a=1,b=1} + \sum_{a=1}^{3}\times\sum_{b=1}^{3}\frac{q_{ia}q_{jb}}{4\pi\varepsilon_0}\frac{1}{r_{ia}r_{jb}} \quad (1)$$

where the van der Waals interaction corresponds to the 12-6-type Lennard-Jones (LJ) potential and ε_{OO} is the energy parameter among the oxygen atoms. To reduce computational cost, water molecules were treated as rigid by constraining the O−H bond and the H−O−H angle. The SHAKE algorithm was applied to water molecules to hold their internal geometry.

To investigate the effects of surface physicochemical properties on boiling performance, we proposed four groups of surfaces, as shown in Figure 1c. Compared with the smooth homogeneous surface, the smooth heterogeneous surface contained square patterns with wetting contrast, and similarly, the rough surface consisted of a substrate and square-pillar arrays that had uniform or hybrid wettability. Notice that the homogeneous surface here could be a hydrophobic substrate with hydrophilic patterns or pillars but also a hydrophilic substrate with hydrophobic patterns or pillars; thus, eight kinds of surfaces were built herein, and they are correspondingly designated as surfaces S_o, S_i, S_{io}, S_{oi}, R_o, R_i, R_{io}, and R_{oi} for the convenience of subsequent description and analyses, as detailed in Table 1.

To endow the solid surface with tunable wettability and improve computation efficiency, the simpler copper-like atoms were adopted to constitute the bottom substrate and the upper wall, whose building block was a face-centered cubic unit cell and the lattice constant was 3.61 Å. The intermolecular interactions between copper-like atoms and water molecules were described by the 12-6 LJ potential, where the energy parameter ε_{CuO} could be changed to adjust the wettability of the solid surface. The visualization and evaluation for the intrinsic wetting capacity of the hydrophilic surface and the hydrophobic surface studied here are shown in Figure 1d. By extracting the droplet profile and using the circle fitting method, the intrinsic contact angles were calculated to be 75.2° and 116.3°, respectively. The embedded atom model (EAM) potential was employed to describe the heat conduction in the heating substrate and the cooling wall. Surfaces were treated as shown in the partially enlarged drawing of Figure 1b, the atoms in the outermost layer were frozen to prevent surface deformation, the three middle layers acted as the heat source through applying a thermostat, and the remaining conduction layers transported the energy between the heat source and the liquid film.

After the model energy was minimized, we first conducted a pre-equilibration. In this stage, to obtain a stable state of the gas−liquid−solid triple-phase coexistence at a temperature of 373 K, the entire system was integrated in an NVT ensemble with a Nosé−Hoover thermostat for 1.0 ns. In the following main simulation stage, the temperature of the bottom substrate (heat source) and the upper wall (cold source) was respectively controlled at 500 K and 300 K by the Langevin method, and the remaining parts were integrated with the

https://doi.org/10.1021/acs.langmuir.2c00276
Langmuir 2022, 38, 6352−6362

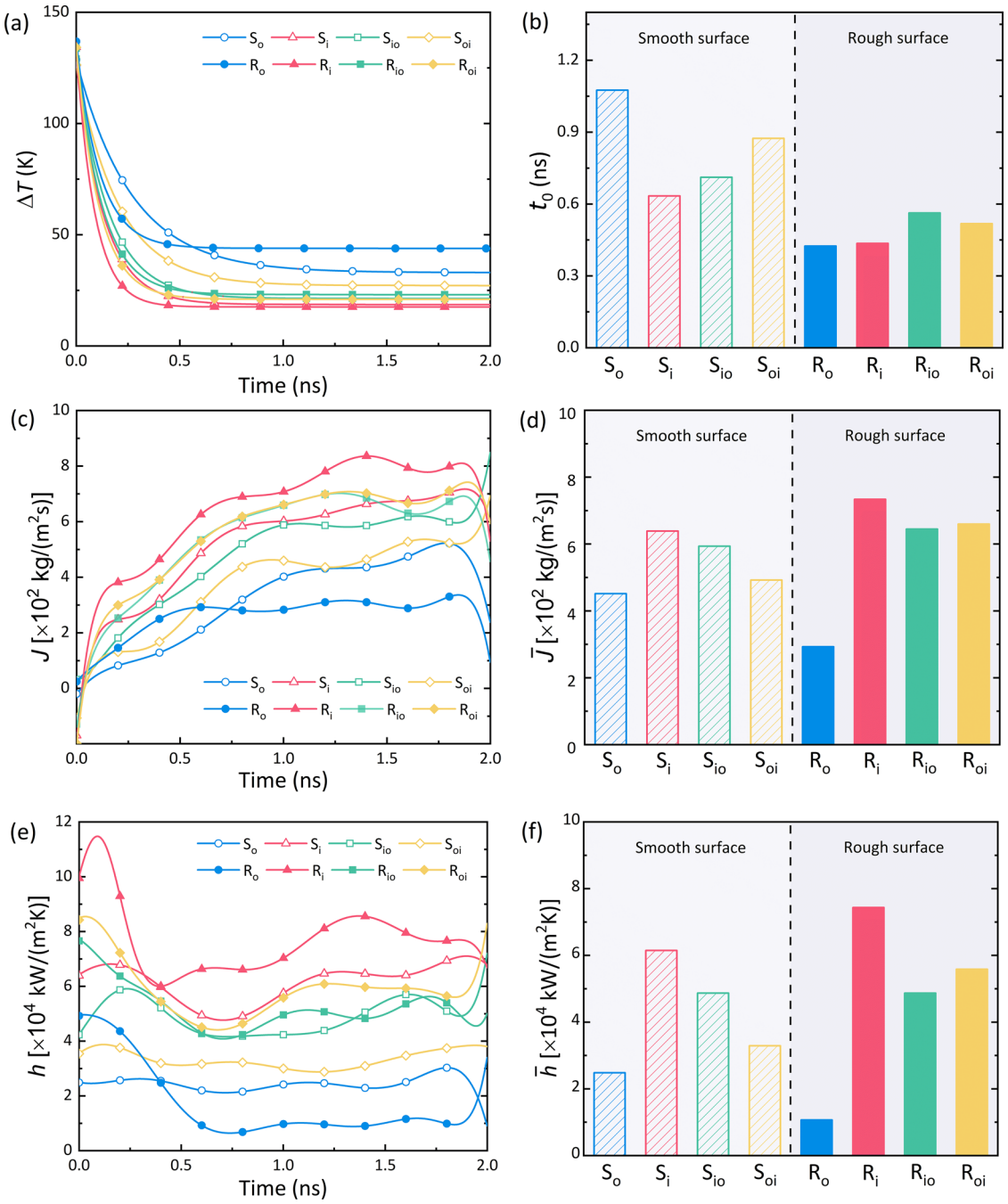

Figure 4. Comparison of boiling heat transfer and mass transfer performances for different surfaces. (a) Variation of the temperature difference ΔT between the heating substrate and the liquid film, its variation tendency can be used to determine the onset time of stable boiling. (b) Onset time of stable boiling t_0 for each surface. (c) Temporal evolution of mass flux J. (d) Average mass flux $\overline{J}$ of each surface during the stable boiling stage. (e) Temporal evolution of the surface heat transfer coefficient h. (f) Average heat transfer coefficient $\overline{h}$ of each surface during the stable boiling stage.

NVE ensemble to simulate the transfer process combining heat and mass. The simulation data and views were collected in this 2.0 ns NVE process. All the MD simulations were performed using the open-source code LAMMPS[53] and visualized by the package OVITO.[54] The long-range electrostatic interactions were calculated by the particle−particle−particle mesh (PPPM) method with a relative accuracy of 1×10^{-5}. The van der Waals and Coulombic interactions were truncated at 12 Å and 10 Å, respectively. The particle motion equation was solved by the common velocity Verlet algorithm, and the time step was set to 1 fs.

3. RESULTS AND DISCUSSION

3.1. Thin-Film Boiling Simulations. In this section, the surface R_{io} was selected as an example to discuss the simulation results. Figure 2a,b shows the liquid film boiling process from different views. To save space and capture the details of the triple-phase interface, only the bottom half of the simulation domain was visualized, and the gas−liquid interface was constructed using the α-shape algorithm with a probe sphere radius of 5 Å. It is seen that the free liquid surface fluctuates gradually with the liquid film being heated, which indicates the increasingly intense motion of water molecules. After a certain

https://doi.org/10.1021/acs.langmuir.2c00276
Langmuir 2022, 38, 6352−6362

amount of time, a nanopillar initially immersed in liquid is exposed above the lowered water level, and as the liquid further vaporizes, this exposed area expands to other adjacent nanopillars and extend from the structure top to the structure valley, leading to a local dry-out phenomenon eventually, as is shown in the snapshot at 2 ns.

To probe the fluid flow and thermal characteristics, the entire simulation region was divided into many cubic boxes with a side length of 5 Å, and the time-averaged local properties of each box, including fluid density, temperature, and velocity, were calculated and recorded at regular intervals (the local properties were sampled every 5 fs, and their time-averaged values were calculated and printed at intervals of 5 ps from 200 samples). Considering the difficulty of directly observing the internal fluid characteristics from an intricate three-dimensional (3d) view, a $y-z$ central cross section (x_0 = 56 Å) was chosen to plot fluid density contours, temperature contours, and velocity fields, which are shown in Figure 2c,d (see the enlarged view of the velocity field images in the Supporting Information). It is obviously observed that the average temperature in the main part of the fluid increases and the corresponding average density decreases as the boiling process progresses, although the spatial distributions of temperature and density are nonuniform. Furthermore, the initially slow fluid flow becomes intense gradually when the liquid film is heated, but in general, the fluid on the gas–liquid interface is more active, indicating that a strong mass transfer exists on the free liquid surface.

To test the simulation reliability and get the basic properties of the system, we performed calculations on this phase change process, whose temporal variations of thermophysical characterizations are shown in Figure 3. In the pre-equilibrium stage (Figure 3a), the liquid temperature basically stabilizes at a setting value of 373 K, while the vapor pressure increases first and finally fluctuates around a constant, namely, the saturation vapor pressure of water P_s. Through fitting the simulation results, we obtained a smooth variation curve of vapor pressure, and the value of P_s at 373 K is calculated to be 0.087 MPa according to the fitting data, which is close to the experimental value. In the phase change stage (Figure 3b), the hot substrate, whose temperature T_s stabilizes at 500 K from the beginning to the end, heats the liquid film and increases its temperature T_l to about 477 K. Correspondingly, the vapor pressure first increases rapidly, reaches a peak, and then declines slowly. It should be noted that there exists a temperature gradient along the direction of heat transfer, so the average temperature of the liquid in every layer is different. Here, to unify the calculation of each case, T_l was calculated as the average liquid temperature in the middle layer with a thickness of 5 Å.

The evaluation for heat and mass transfer performance was obtained from the water molecule change in the vapor region and the heat absorption from the substrate to the liquid; to reduce the influence of strong mass exchange near the gas–liquid interface, only water molecules in the region that is more than 15 Å above the initial free liquid surface were counted. Figure 3c shows the variation of the number of evaporated molecules N_w and absorbed heat Q; both of them reach a nearly linear growth state after the initiation stage, indicating entering a steady phase change stage. Based on the change rate of these data, the mass flux J and heat flux q of the system were respectively calculated as $J = \frac{m_0}{A}\cdot\frac{\partial N_w}{\partial t}$ and $q = \frac{1}{A}\cdot\frac{\partial Q}{\partial t}$ (shown in the inset of Figure 3d), where m_0 and A denote the mass of a single water molecule and the projective area of the substrate (125.44 nm^2). Through fitting the simulation data of T_s and T_l, the temperature difference $\Delta T = T_s - T_l$ was calculated, whose time history is shown in the inset of Figure 3d. The evaluation parameter for heat transfer performance of the system, i.e., the surface heat transfer coefficient (HTC), was calculated by using the following formula: $h = q/\Delta T$, whose variation tendency is shown in Figure 3d. Although the values of both q and ΔT are attenuated over time, there is a high HTC at the initial moment due to the large heat flux in the initiation stage. Soon afterward, the HTC decreases gradually and fluctuates in a certain range when the phase transition process tends to be steady, and the corresponding variations of the heat flux and temperature difference are also slight in this stable boiling stage.

3.2. Effects of Surface Physicochemical Properties on Boiling Performance. Simulation results of all cases are presented and discussed here to systematically analyze the effects of surface physicochemical properties (roughness and wettability) on boiling, especially on the heat and mass transfer performance. The aforementioned results suggest that the phase change process takes a certain period of time to stabilize; thus, the transition from the initiation stage to the stable boiling stage can be denoted by an onset time, which would quantify how quickly the boiling phenomenon happens. The onset time t_0 of stable boiling was extracted from the crossover point between the initiation stage and the stable stage, which was defined as the critical point whose ΔT value increased by 5% compared with the final value of ΔT. Figure 4a,b shows the temporal variation of ΔT and the value of t_0 for each corresponding surface. It can be found that the rapidity of the change in all cases is disparate, notwithstanding the similar exponential trend for ΔT. For the onset time of stable boiling obtained from the $\Delta T-t$ curve, rough surfaces have a lower t_0 than smooth surfaces on whether an overall or individual level (i.e., $R_o < S_o$, $R_i < S_i$, $R_{io} < S_{io}$, and $R_{oi} < S_{oi}$), indicating that rough structures promote a quicker-response boiling process, which is more desired in the industrial manufacturing field.

Figure 4c presents the calculated results of mass fluxes J; there is an obvious climb in the initiation stage, but the whole trends are intricate and fluctuant for all cases, which makes it hard to make a comparison directly. Hence, the average mass flux $\bar{J}$ is introduced here, which is obtained by averaging the value of J only in the stable boiling stage and is more suitable to estimate the overall mass transfer performance for each surface. As shown in Figure 4d, rough surfaces have larger mass fluxes than corresponding smooth surfaces (i.e., $R_i > S_i$, $R_{io} > S_{io}$, and $R_{oi} > S_{oi}$) apart from the surface R_o, with increases of 14.87%, 8.65%, and 34.03%, respectively, and the value of mass flux for the surface R_i is as high as 7.34×10^2 kg/(m^2·s). The results suggest that for nanoscale thin-film boiling, a rough hydrophilic surface possesses the highest mass flux, while the combination of a hydrophobic substrate and hydrophilic structures may induce the greatest improvement in mass transfer performance.

Figure 4e demonstrates the calculated results of the heat transfer coefficient h; there is a high HTC in the initiation stage, especially for rough surfaces, and then, the HTC decreases gradually and fluctuates when entering the stable boiling stage. Similarly, to directly compare and quantitatively estimate the overall heat transfer performance of each surface, we calculated the average value of the HTC only in the stable

https://doi.org/10.1021/acs.langmuir.2c00276
Langmuir 2022, 38, 6352−6362

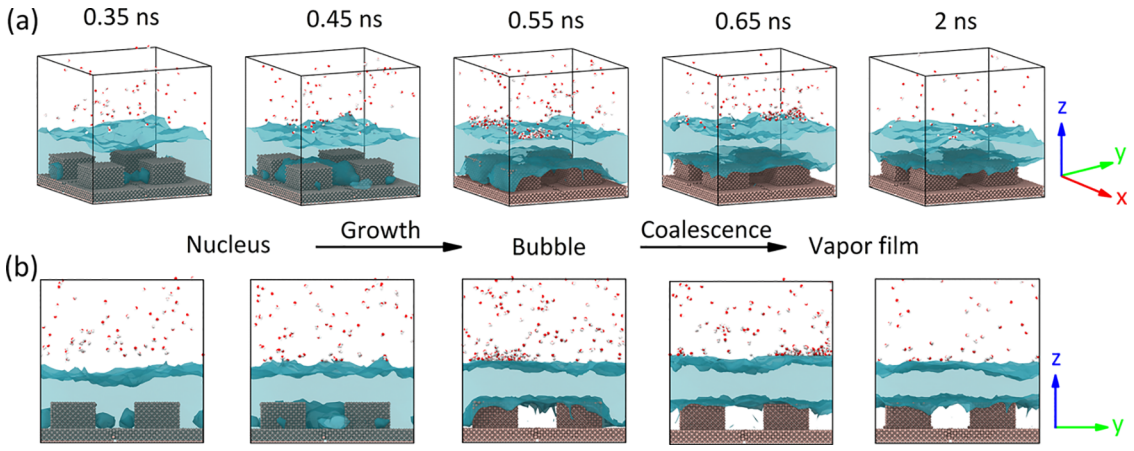

Figure 5. Representative snapshots of the boiling regime for the surface R_o (rough surface with uniform hydrophobicity). The top half of the simulation domain is hidden, and the gas−liquid interface is visualized to intuitively observe the shape and location change of bubbles during the boiling process. (a) Orthogonal view and (b) side view.

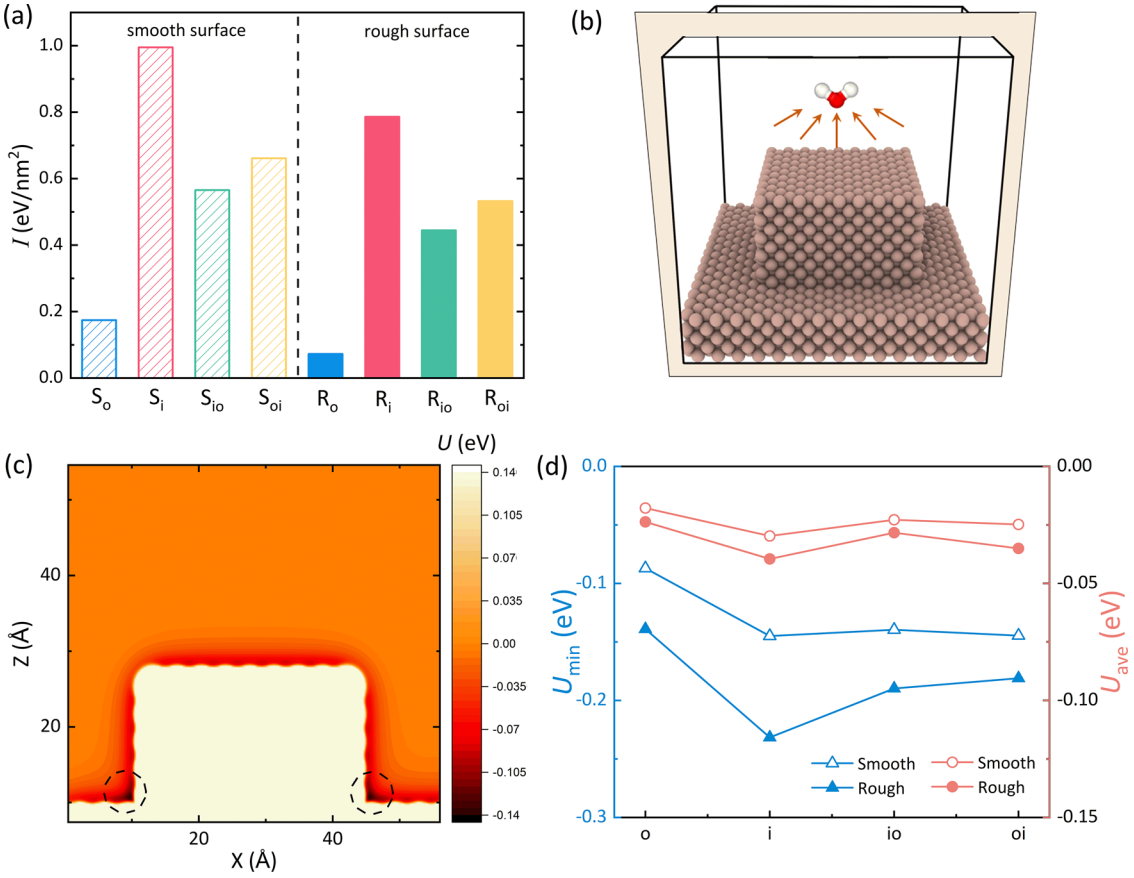

Figure 6. (a) Interaction energy intensity I of each surface. (b) Schematic for calculating the potential energy of a water molecule. (c) Potential energy distribution of a water molecule on the structural unit of the rough hydrophobic surface R_o, the dashed circles mark the region with the low value of potential energy. (d) Average potential energy U_{ave} and the minimum potential energy U_{min} of a water molecule on each surface.

stage, which is termed as the average heat transfer coefficient $\overline{h}$. As shown in Figure 4f, rough surfaces have a larger HTC than corresponding smooth surfaces (i.e., $R_i > S_i$, $R_{io} > S_{io}$, and $R_{oi} > S_{oi}$) apart from the surface R_o, with increases of 20.89%, 0.17%, and 69.65%, respectively. Among them, the value of $\overline{h}$ for the surface R_i is as high as 7.43×10^4 kW/(m^2·K), and the corresponding heat flux reaches to about 130 kW/cm^2, which is higher by about 100 times than that of the micrometer-scale thin-film boiling[31] and shows great potential in high-heat flux removal.

The above results indicate that rough structures enhance both the mass flux and the heat transfer performance of the boiling process, except for rough hydrophobic surfaces. According to our observation, a bubble forms only on the rough hydrophobic surface R_o (refer to the visualization of each simulation case in the Supporting Information); the phenomenon is arrestive because promoting the bubble

https://doi.org/10.1021/acs.langmuir.2c00276
Langmuir 2022, 38, 6352−6362

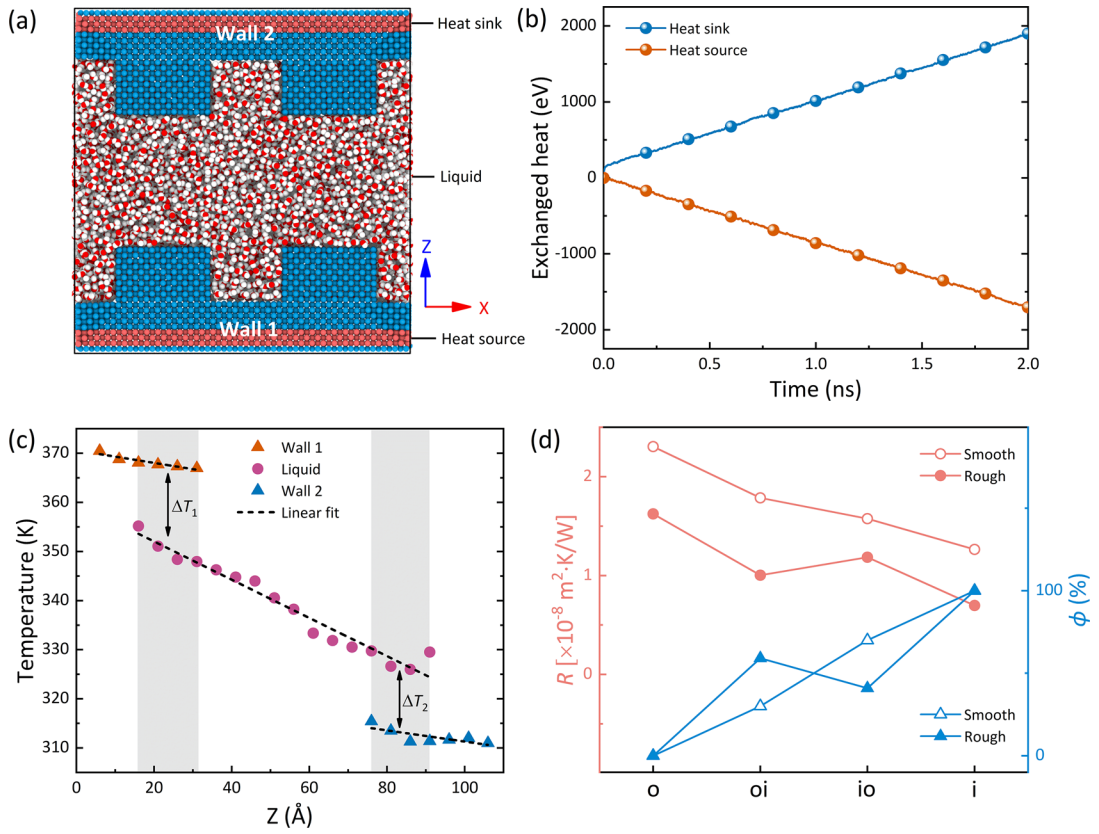

Figure 7. Calculation and comparison of the interfacial thermal resistance for different surfaces. The simulation model and methods are illustrated by an example of the surface R_i. (a) Measurement system configuration in the vertical section. (b) Evolution of the accumulative exchanged heat in the heat source and the heat sink. (c) System temperature distribution along the z direction, where shadow areas denote the solid−liquid overlapping regions. (d) Interfacial thermal resistance R and area proportion ϕ of the hydrophilic region for each surface.

formation is essential to enhance the macroscale boiling heat transfer; however, this is not the case in the simulated nanoscale system, where the rough surfaces that inhibit the bubble nucleation have a better performance instead. Figure 5 shows the unique boiling regime of the rough hydrophobic surface R_o. Bubble nuclei first originate at the base corner of nanopillars and gradually grow into nanobubbles, but due to the weak pinning effect of the hydrophobic surface, further growth and coalescence of bubbles prompt the dramatic triple-phase contact line expansion from the structure base to the structure valley to the structure top and finally generate a vapor film trapped between the liquid and the substrate, which can inhibit heat and mass exchange and induce heat transfer deterioration. Therefore, pinning the bubble contact line and even suppressing bubble formation are conductive to enhancing the heat and mass performance of thin liquid films.

To understand the physical mechanism of bubble nucleation from a molecular view, we computed the intensity I of solid−liquid interaction energy (simulation details are in Section S3 of the Supporting Information), which represents an energy per unit area[28,43] to separate a group of particles into two parts and can be used to evaluate the energy barrier of bubble nucleation. As shown in Figure 6a, the value of I is manipulated by the surface wettability and structures; rough surfaces have a lower interaction energy intensity than corresponding smooth surfaces (i.e., $R_o < S_o$, $R_i < S_i$, $R_{io} < S_{io}$, and $R_{oi} < S_{oi}$), with decreases of 58.35%, 21.03%, 21.40%, and 19.47%, respectively. According to the simulation data, we found that this is because the extra solid atoms from structures greatly reduce the potential energy and further decrease the total energy of the system (as shown in Figure S4 of the Supporting Information). Due to the fact that the nucleation path follows the principle of minimum free energy, the rough hydrophobic surface R_o with the lowest interaction intensity is favorable for bubble nucleation, while the bubbles need to absorb more heat to break the nucleation energy barrier for other surfaces.

Figure 5 shows that bubble nuclei first originate at the base corner of nanopillars on the surface R_o. To analyze the behaviors of bubble nucleation, we computed the potential energy[28,45] U of one single water molecule at the solid−liquid interface. Taking the surface R_o for example, as shown in Figure 6b, we chose a structural unit (one single pillar) and calculated the potential energy between one single water molecule and all solid atoms according to the 12-6 LJ potential function. After obtaining the values of U in various positions, an $x-z$ central cross section was selected to plot the potential energy distribution of a water molecule on the surface R_o, as shown in Figure 6c, and the potential energy distribution on other surfaces is shown in Figure S5 of the Supporting Information. The potential energy with a negative value represents that the water molecules are restricted; obviously, the potential restriction on the liquid molecules is larger than that on the vapor molecules; thus, the liquid molecules need to absorb enough heat from the surface to vaporize. Furthermore, it is seen that there exist low-potential-energy regions at each solid−liquid interface; their different locations cause the potential energy distributions to be varied. Especially for the surface R_o in Figure 6c, the base corner regions marked by

https://doi.org/10.1021/acs.langmuir.2c00276
Langmuir 2022, 38, 6352−6362

dashed circles have the locally lowest potential energy, which indicates that the interaction between the liquid molecules and the surface is the strongest; therefore, the liquid molecules in these regions can absorb more thermal energy to form bubble nuclei relatively easily. Based on the data of potential energy distribution, we calculated the average potential energy U_{ave} and the minimum potential energy U_{min} of a water molecule (calculation details are in Section S4 of the Supporting Information), as shown in Figure 6d. The results indicate that the potential energy changes with the surface physicochemical properties; rough surfaces have a lower U_{ave} and U_{min} than corresponding smooth surfaces, and compared to the uniformly hydrophobic surfaces, the addition of hydrophilic regions also reduces the values of U_{ave} and U_{min}.

3.3. Mechanism Analysis of Boiling Enhancement. For a nanoscale system involving heat transfer, the interfacial thermal resistance (ITR)[44,55] at the solid−liquid interface is a significant factor. To elucidate the underlying mechanism of regulation effects of surface physicochemical properties on heat and mass transfer efficiency, another set of simulations were conducted to calculate the interfacial thermal resistance R of each surface. Taking the surface R_i for example, the liquid is sandwiched between two identical surfaces called wall 1 and wall 2, and the distance between the opposite walls is larger than the cutoff radius of 12 Å, as shown in Figure 7a. Surfaces were treated in the same way as mentioned above; the three middle layers work as a heat source or a heat sink through applying a thermostat. Similarly, an NVT ensemble was first applied to the whole system at 340 K for 1.0 ns, and then, the ensemble was switched to NVE while the temperatures of the heat source and the heat sink were respectively controlled at 370 K and 310 K for 2.0 ns, introducing a temperature gradient into the system.

According to the formula $R = \Delta T/q$, the interfacial temperature difference and heat flux are requirements in the calculation of ITR. Figure 7b demonstrates the variation of accumulative exchanged heat, whose positive and negative values respectively represent heat absorption and heat release. Based on the linear fitting results of exchanged heat, the heat flux of the heat source q_1 and the heat flux of the heat sink q_2 were computed with the same method as mentioned above, and their approximately equal values prove the simulation reliability. To get the value of ΔT, the entire system was divided into many equally sized one-dimensional bins along the z direction, and the time-averaged temperature of each bin was calculated and recorded at regular intervals. Figure 7c shows the stable-state temperature distribution of the system in the vertical direction; a temperature drop is obviously observed at the solid−liquid interfaces, and the interfacial temperature differences of wall 1 and wall 2 are called ΔT_1 and ΔT_2 here. After segmentally linear fitting of the temperature data, ΔT_1 and ΔT_2 can be directly obtained according to the fitting data at solid−liquid interfaces for smooth surfaces, and for rough surfaces, ΔT_1 and ΔT_2 are the average temperature differences between solid and liquid at overlapping regions (as shown in the shadow areas of Figure 7c).

Based on the values of q_1, q_2, ΔT_1, and ΔT_2, the interfacial thermal resistances R_1 and R_2 were calculated and averaged to get the final value of R. Figure 7d shows R of each kind of surface; the results reflect that the existence of rough structures reduces the interface thermal resistance. By comparison, it was found that heat fluxes are considerably improved and the temperature drops shrink slightly for rough surfaces; this is because structures increase the interfacial area transferring heat. It is important to note that the interfacial thermal resistances of uniformly hydrophilic surfaces and uniformly hydrophobic surfaces are maximum and minimum, respectively, whether on smooth cases or rough cases. It is demonstrated that the stronger hydrophilicity endows the smooth surface with lower interfacial thermal resistance;[56] however, the results here suggest that this rule is not limited to the smooth homogeneous surface, but it can also be applied to chemically and physically heterogeneous surfaces with hydrophilic regions. Furthermore, the area proportion ϕ of the hydrophilic region was calculated and is recorded in Figure 7d, where the variation of R is negatively correlated with ϕ. The above results indicate that the boiling enhancement resulting from surface physicochemical properties is essentially attributed to the reduction of interfacial thermal resistance, and increasing surface roughness, enhancing surface wettability, and improving the area proportion of the hydrophilic region are three effective ways to reduce the interfacial thermal resistance.

4. CONCLUSIONS

In summary, we have studied the nanoscale thin-film boiling processes on various heterogeneous surfaces by classical MD simulations, and the effects of surface physicochemical properties on boiling were evaluated and analyzed. The results show that nanoscale thin-film boiling has excellent heat and mass transfer performance due to the inhibition of bubble formation, which is completely different from macroscale boiling. Nanostructures promote a quicker-response and more efficient thin-film boiling process, and the heat flux and mass flux on a rough hydrophilic surface respectively reach ultrahigh values up to 130 kW/cm^2 and 734 kg/(m^2·s), achieving two orders of magnitude enhancement. However, the rough hydrophobic surface induces heat transfer deterioration because the vapor film coalescing from nanobubbles obstructs the heat exchange between the liquid and the surface. Furthermore, compared with the congeneric smooth surface, the combination of a hydrophobic substrate and hydrophilic structures improves the heat and mass transfer performance most greatly. This regulatory effect resulting from surface physicochemical properties is essentially attributed to the change of interfacial thermal resistance. Increasing surface roughness, enhancing surface wettability, and increasing the area proportion of the hydrophilic region can all reduce the overall interfacial resistance and further improve the heat and mass transfer efficiency. Findings of this work enrich our understanding of the nanoscale liquid−vapor phase change and provide a reference for the optimized design of surfaces utilized for high-heat flux removal through vaporization processes.

■ ASSOCIATED CONTENT

Supporting Information

The Supporting Information is available free of charge at https://pubs.acs.org/doi/10.1021/acs.langmuir.2c00276.

Enlarged view of the velocity field images; visualization result of each simulation case; calculation method of the interaction energy intensity; potential energy distribution of each surface (PDF)

https://doi.org/10.1021/acs.langmuir.2c00276
Langmuir 2022, 38, 6352−6362

AUTHOR INFORMATION

Corresponding Authors

Shan Gao − *School of Energy and Power Engineering, Jiangsu University, Zhenjiang 212013, China;* orcid.org/0000-0003-1957-9107; Email: s_gao@ujs.edu.cn

Zhichun Liu − *School of Energy and Power Engineering, Huazhong University of Science and Technology, Wuhan 430074, China;* orcid.org/0000-0001-9645-3052; Email: zcliu@hust.edu.cn

Authors

Jian Qu − *School of Energy and Power Engineering, Jiangsu University, Zhenjiang 212013, China*

Wei Liu − *School of Energy and Power Engineering, Huazhong University of Science and Technology, Wuhan 430074, China*

Complete contact information is available at: https://pubs.acs.org/10.1021/acs.langmuir.2c00276

Notes

The authors declare no competing financial interest.

ACKNOWLEDGMENTS

The authors thank the National Supercomputer Center in Tianjin for providing computing resources. This study was supported by the National Natural Science Foundation of China (nos. 52076088 and 51576091).

REFERENCES

(1) Agrawal, P.; Wells, G. G.; Ledesma-Aguilar, R.; McHale, G.; Sefiane, K. Beyond Leidenfrost levitation: A thin-film boiling engine for controlled power generation. *Appl. Energy* **2021**, *287*, 116556.

(2) Sinha-Ray, S.; Zhang, W.; Stoltz, B.; Sahu, R. P.; Sinha-Ray, S.; Yarin, A. L. Swing-like pool boiling on nano-textured surfaces for microgravity applications related to cooling of high-power micro-electronics. *npj Microgravity* **2017**, *3*, 1−9.

(3) Sadaghiani, A. K.; Saadi, N. S.; Parapari, S. S.; Karabacak, T.; Keskinoz, M.; Koşarac, A. Boiling heat transfer performance enhancement using micro and nano structured surfaces for high heat flux electronics cooling systems. *Appl. Therm. Eng.* **2017**, *127*, 484−498.

(4) Besnard, C.; Allemand, A.; David, P.; Léon, J. F.; Maillé, L. An original concept for the synthesis of an oxide coating: The film boiling process. *J. Eur. Ceram. Soc.* **2021**, *41*, 3013−3018.

(5) Zhang, C.; Wang, D.; Yang, J.; Zhang, W.; Sun, Q.; Yu, F.; Fan, Y.; Li, Y.; Chen, L.; Deng, X. Charge Density Gradient Propelled Ultrafast Sweeping Removal of Dropwise Condensates. *J Phys Chem B* **2021**, *125*, 1936−1943.

(6) Xu, W.; Zheng, H.; Liu, Y.; Zhou, X.; Zhang, C.; Song, Y.; Deng, X.; Leung, M.; Yang, Z.; Xu, R. X.; Wang, Z. L.; Zeng, X. C.; Wang, Z. A droplet-based electricity generator with high instantaneous power density. *Nature* **2020**, *578*, 392−396.

(7) Lambley, H.; Schutzius, T. M.; Poulikakos, D. Superhydrophobic surfaces for extreme environmental conditions. *Proc. Natl. Acad. Sci. U. S. A.* **2020**, *117*, 27188−27194.

(8) Chen, H.; Li, L.; Wang, Y.; Guo, Y. Heat transfer enhancement in nucleate boiling on micropillar-arrayed surfaces with time-varying wettability. *Appl. Therm. Eng.* **2022**, *200*, 117649.

(9) Zhang, L.; Zhu, Y.; Lu, Z.; Zhao, L.; Bagnall, K. R.; Rao, S. R.; Wang, E. N. Characterization of thin film evaporation in micropillar wicks using micro-Raman spectroscopy. *Appl. Phys. Lett.* **2018**, *113*, 163701.

(10) Dai, X.; Huang, X.; Yang, F.; Li, X.; Sightler, J.; Yang, Y.; Li, C. Enhanced nucleate boiling on horizontal hydrophobic-hydrophilic carbon nanotube coatings. *Appl. Phys. Lett.* **2013**, *102*, 161605.

(11) Lin, Y.; Chu, F.; Ma, Q.; Wu, X. Gyroscopic rotation of boiling droplets. *Appl. Phys. Lett.* **2021**, *118*, 221601.

(12) Li, D.; Wu, G. S.; Wang, W.; Wang, Y. D.; Liu, D.; Zhang, D. C.; Chen, Y. F.; Peterson, G. P.; Yang, R. Enhancing flow boiling heat transfer in microchannels for thermal management with monolithically-integrated silicon nanowires. *Nano Lett.* **2012**, *12*, 3385−3390.

(13) Li, J.; Fu, W.; Zhang, B.; Zhu, G.; Miljkovic, N. Ultrascalable Three-Tier Hierarchical Nanoengineered Surfaces for Optimized Boiling. *ACS Nano* **2019**, *13*, 14080−14093.

(14) Li, Y.; Chen, H.; Xiao, S.; Alibakhshi, M. A.; Lo, C. W.; Lu, M. C.; Duan, C. Ultrafast Diameter-Dependent Water Evaporation from Nanopores. *ACS Nano* **2019**, *13*, 3363−3372.

(15) Allred, T. P.; Weibel, J. A.; Garimella, S. V. Enabling Highly Effective Boiling from Superhydrophobic Surfaces. *Phys. Rev. Lett.* **2018**, *120*, 174501.

(16) Cho, H. J.; Preston, D. J.; Zhu, Y.; Wang, E. N. Nanoengineered materials for liquid−vapour phase-change heat transfer. *Nat. Rev. Mater.* **2017**, *2*, 1−17.

(17) Wen, R.; Li, Q.; Wang, W.; Latour, B.; Li, C. H.; Li, C.; Lee, Y.-C.; Yang, R. Enhanced bubble nucleation and liquid rewetting for highly efficient boiling heat transfer on two-level hierarchical surfaces with patterned copper nanowire arrays. *Nano Energy* **2017**, *38*, 59−65.

(18) Dai, X.; Wang, P.; Yang, F.; Li, X.; Li, C. Decoupling the influence of surface structure and intrinsic wettability on boiling heat transfer. *Appl. Phys. Lett.* **2018**, *112*, 253901.

(19) Long, J.; Liu, Z.; Lin, H.; Li, Y.; Cao, Z.; Zhang, Z.; Xie, X. Pool Boiling Heat Transfer and Bubble Dynamics Over V-Shaped Microchannels and Micropyramids: Does High Aspect Ratio Always Benefit Boiling? *Appl. Therm. Eng.* **2021**, *201*, 117796.

(20) Li, J.; Zhu, G.; Kang, D.; Fu, W.; Zhao, Y.; Miljkovic, N. Endoscopic Visualization of Contact Line Dynamics during Pool Boiling on Capillary-Activated Copper Microchannels. *Adv. Funct. Mater.* **2021**, *31*, 2006249.

(21) Zhang, Y.; Wei, J.; Xue, Y.; Kong, X.; Zhao, J. Bubble dynamics in nucleate pool boiling on micro-pin-finned surfaces in microgravity. *Appl. Therm. Eng.* **2014**, *70*, 172−182.

(22) Mohanty, R. L.; Das, M. K. A critical review on bubble dynamics parameters influencing boiling heat transfer. *Renewable and Sustainable Energy Reviews* **2017**, *78*, 466−494.

(23) Yamamoto, T.; Matsumoto, M. Initial stage of nucleate boiling: molecular dynamics investigation. *Journal of Thermal Science and Technology* **2012**, *7*, 334−349.

(24) Mao, Y.; Zhang, Y. Molecular dynamics simulation on rapid boiling of water on a hot copper plate. *Appl. Therm. Eng.* **2014**, *62*, 607−612.

(25) Zhang, S.; Hao, F.; Chen, H.; Yuan, W.; Tang, Y.; Chen, X. Molecular dynamics simulation on explosive boiling of liquid argon film on copper nanochannels. *Appl. Therm. Eng.* **2017**, *113*, 208−214.

(26) R., Diaz; Z., Guo, *Molecular dynamics study of contact angle effect on maximum critical heat flux in nano-patterned pool boiling*; ASTFE Digital Library: Begel House Inc., (2017).

(27) Diaz, R.; Guo, Z. A molecular dynamics study of phobic/philic nano-patterning on pool boiling heat transfer. *Heat Mass Transfer* **2017**, *53*, 1061−1071.

(28) Bai, P.; Zhou, L.; Huang, X.; Du, X. Molecular Insight into Bubble Nucleation on the Surface with Wettability Transition at Controlled Temperatures. *Langmuir* **2021**, *37*, 8765−8775.

(29) Wen, R.; Xu, S.; Lee, Y.-C.; Yang, R. Capillary-driven liquid film boiling heat transfer on hybrid mesh wicking structures. *Nano Energy* **2018**, *51*, 373−382.

(30) Bigham, S.; Fazeli, A.; Moghaddam, S. Physics of micro-structures enhancement of thin film evaporation heat transfer in microchannels flow boiling. *Sci. Rep.* **2017**, *7*, 44745.

(31) Wang, Q.; Chen, R. Ultrahigh Flux Thin Film Boiling Heat Transfer Through Nanoporous Membranes. *Nano Lett.* **2018**, *18*, 3096−3103.

(32) Gao, S.; Liao, Q.; Liu, W.; Liu, Z. Effects of Solid Fraction on Droplet Wetting and Vapor Condensation: A Molecular Dynamic Simulation Study. *Langmuir* **2017**, *33*, 12379−12388.

(33) Hubao, A.; Yang, Z.; Hu, R.; Chen, Y. F.; Yang, L. Effect of Solid−Liquid Interactions on Substrate Wettability and Dynamic

Spreading of Nanodroplets: A Molecular Dynamics Study. *J. Phys. Chem. C* **2020**, *42*, 23260−23269.
(34) Gao, S.; Liao, Q.; Liu, W.; Liu, Z. Nanodroplets Impact on Rough Surfaces: A Simulation and Theoretical Study. *Langmuir* **2018**, *34*, 5910−5917.
(35) Wang, T.; Ai, L.; Zhou, Y.; Chen, M. Numerical Simulation of Supercooled Water Droplets Impacting Ice with Rapid Crystal Growth Taken into Consideration. *Langmuir* **2020**, *36*, 5466−5473.
(36) Wang, Y.-B.; Wang, X.-D.; Yang, Y.-R.; Chen, M. The Maximum Spreading Factor for Polymer Nanodroplets Impacting a Hydrophobic Solid Surface. *The Journal of Physical Chemistry C* **2019**, *123*, 12841−12850.
(37) Li, H.; Zhang, K. Dynamic behavior of water droplets impacting on the superhydrophobic surface: Both experimental study and molecular dynamics simulation study. *Appl. Surf. Sci.* **2019**, *498*, 143793.
(38) Gao, S.; Liao, Q.; Liu, W.; Liu, Z. Coalescence-Induced Jumping of Nanodroplets on Textured Surfaces. *J. Phys. Chem. Lett.* **2018**, *9*, 13−18.
(39) Perumanath, S.; Borg, M. K.; Sprittles, J. E.; Enright, R. Molecular physics of jumping nanodroplets. *Nanoscale* **2020**, *12*, 20631−20637.
(40) Gao, S.; Long, J.; Liu, W.; Liu, Z. Evaporation-Induced Wetting Transition of Nanodroplets on Nanopatterned Surfaces with Concentric Rings: Surface Geometry and Wettability Effects. *Langmuir* **2019**, *35*, 9546−9553.
(41) Wu, X.; Yang, Z.; Duan, Y. Molecular dynamics simulation on evaporation of a suspending difluoromethane nanodroplet. *Int. J. Heat Mass Transfer* **2020**, *158*, 120024.
(42) Liu, R.; Liu, Z. Rapid thermal transport at rough solid-fluid interface: Evaporation and explosive boiling on concave nanostructure. *Int. J. Heat Mass Transfer* **2020**, *154*, 119676.
(43) Cao, Q.; Cui, Z.; Shao, W. Optimization Method for Grooved Surface Structures Regarding the Evaporation Heat Transfer of Ultrathin Liquid Films at the Nanoscale. *Langmuir* **2020**, *36*, 2802−2815.
(44) Liu, H.; Ahmad, S.; Chen, J.; Zhao, J. Molecular dynamics study of the nanoscale boiling heat transfer process on nanostructured surfaces. *International Communications in Heat and Mass Transfer* **2020**, *119*, 104963.
(45) Chen, Y. J.; Chen, X. J.; Yu, B.; Zou, Y.; Tao, W. Q. Molecular Dynamics Study of Bubble Nucleation on an Ideally Smooth Substrate. *Langmuir* **2020**, *36*, 13725−13734.
(46) Pu, J. H.; Wang, S. K.; Sun, J.; Wang, W.; Wang, H. S. Stable and Efficient Nanofilm Pure Evaporation on Nanopillar Surfaces. *Langmuir* **2021**, *37*, 3731−3739.
(47) Zhang, L.; Xu, J.; Liu, G.; Lei, J. Nucleate boiling on nanostructured surfaces using molecular dynamics simulations. *International Journal of Thermal Sciences* **2020**, *152*, 106325.
(48) Gao, S.; Liu, W.; Liu, Z. Tuning nanostructured surfaces with hybrid wettability areas to enhance condensation. *Nanoscale* **2019**, *11*, 459−466.
(49) Du, B.; Cheng, Y.; Yang, S.; Xu, W.; Lan, Z.; Wen, R.; Ma, X. Preferential Vapor Nucleation on Hierarchical Tapered Nanowire Bunches. *Langmuir* **2021**, *37*, 774−784.
(50) Pu, J. H.; Sun, J.; Sheng, Q.; Wang, W.; Wang, H. S. Dependences of Formation and Transition of the Surface Condensation Mode on Wettability and Temperature Difference. *Langmuir* **2020**, *36*, 456−464.
(51) Guo, L.; Tang, G. H.; Kumar, S. Dynamic Wettability on the Lubricant-Impregnated Surface: From Nucleation to Growth and Coalescence. *ACS Appl. Mater. Interfaces* **2020**, *12*, 26555−26565.
(52) Hu, H.; Li, Q.; Liu, S.; Fang, T. Molecular dynamics study on water vapor condensation and infiltration characteristics in nanopores with tunable wettability. *Appl. Surf. Sci.* **2019**, *494*, 249−258.
(53) Plimpton, S. Fast parallel algorithms for short-range molecular dynamics. *J. Comput. Phys.* **1995**, *117*, 1−19.
(54) Stukowski, A. Visualization and analysis of atomistic simulation data with OVITO−the Open Visualization Tool. *Modell. Simul. Mater. Sci. Eng.* **2010**, *18*, No. 015012.
(55) Han, H.; Schlawitschek, C.; Katyal, N.; Stephan, P.; Gambaryan-Roisman, T.; Leroy, F.; Müller-Plathe, F. Solid−liquid interface thermal resistance affects the evaporation rate of droplets from a surface: A study of perfluorohexane on chromium using molecular dynamics and continuum theory. *Langmuir* **2017**, *33*, 5336−5343.
(56) Ge, S.; Chen, M. Temperature dependence of thermal resistance at a solid/liquid interface. *Mol. Phys.* **2013**, *111*, 903−908.

https://doi.org/10.1021/acs.langmuir.2c00276
Langmuir 2022, 38, 6352−6362